nature nanotechnology

Article

https://doi.org/10.1038/s41565-023-01350-1

Every-other-layer dipolar excitons in a spin-valley locked superlattice

Received: 9 September 2022

Accepted: 12 February 2023

Published online: 23 March 2023

Check for updates

Yinong Zhang ¹, Chengxin Xiao ^{2,3}, Dmitry Ovchinnikov¹, Jiayi Zhu¹, Xi Wang 1,4, Takashi Taniguchi 5, Kenji Watanabe 6, Jiagiang Yan, Wang Yao ^{© 2,3} ⋈ & Xiaodong Xu ^{© 1,8} ⋈

Monolayer semiconducting transition metal dichalcogenides possess broken inversion symmetry and strong spin-orbit coupling, leading to a unique spin-valley locking effect. In 2H stacked pristine multilayers, spin-valley locking yields an electronic superlattice structure, where alternating layers correspond to barriers and quantum wells depending on the spin-valley indices. Here we show that the spin-valley locked superlattice hosts a kind of dipolar exciton with the electron and hole constituents separated in an every-other-layer configuration: that is, either in two even or two odd layers. Such excitons become optically bright via hybridization with intralayer excitons. This effect is also manifested by the presence of multiple anti-crossing patterns in the reflectance spectra, as the dipolar exciton is tuned through the intralayer resonance by an electric field. The reflectance spectra further reveal an excited state orbital of the every-other-layer exciton, pointing to a sizable binding energy in the same order of magnitude as the intralayer exciton. As layer thickness increases, the dipolar exciton can form a one-dimensional Bose-Hubbard chain displaying layer number-dependent fine spectroscopy structures.

In van der Waals crystals, layer stacking arrangement plays a critical role in determining the material physical properties. Examples include the localized charge hopping and thus, flat band formation in magic angle twisted graphene^{1,2}; the sign switching of interlayer magnetic coupling between the rhombohedral and monoclinic stacked two-dimensional magnet CrI₃^{3,4}; and the formation of interfacial ferroelectricity in AB/BA stacked hexagonal boron nitride (hBN)⁵⁻⁷. For transition metal dichalcogenides (TMDs), such as WSe₂, its monolayer features a sizable spin splitting at the band edges located at the $\pm K$ valleys at the corners of hexagonal Brillouin zone, where time reversal dictates a valley-contrasted sign of the splitting⁸⁻¹³. Multilayers of the 2H stacking feature the 180° rotation between adjacent layers, which is an operation that swaps the spin states between the valleys (Fig. 1a). Consequently, for a carrier of a given spin-valley index, the dispersion edge alternates between the two split values in even and odd layers. These realize perfect superlattice confinements in the out-of-plane direction (Fig. 1b); for a spin-up carrier in the K valley (K, \uparrow) , the even layers serve as energy barriers defining the odd layers as quantum wells (QWs), while for a carrier with an opposite spin-valley index (K, \downarrow) , the odd and even layers swap their roles 9,14-18.

In such spin valley-configured superlattice, the barrier height corresponds to the spin splitting¹⁸. Use WSe₂ as an example, the spin-orbital coupling-induced spin splitting is as large as ~480 meV in the valence bands 19,20. Therefore, the low-energy holes are well confined

Department of Physics, University of Washington, Seattle, WA, USA. Department of Physics, University of Hong Kong, Hong Kong, China. HKU-UCAS Joint Institute of Theoretical and Computational Physics at Hong Kong, Hong Kong, China. ⁴Department of Chemistry, University of Washington, Seattle, WA, USA. 5International Center for Materials Nanoarchitectonics, National Institute for Materials Science, Tsukuba, Japan. 6Research Center for Functional Materials, National Institute for Materials Science, Tsukuba, Japan. 7 Materials Science and Technology Division, Oak Ridge National Laboratory, Oak Ridge, TN, USA. 8Department of Materials Science and Engineering, University of Washington, Seattle, WA, USA. 🖂 e-mail: wangyao@hku.hk; xuxd@uw.edu

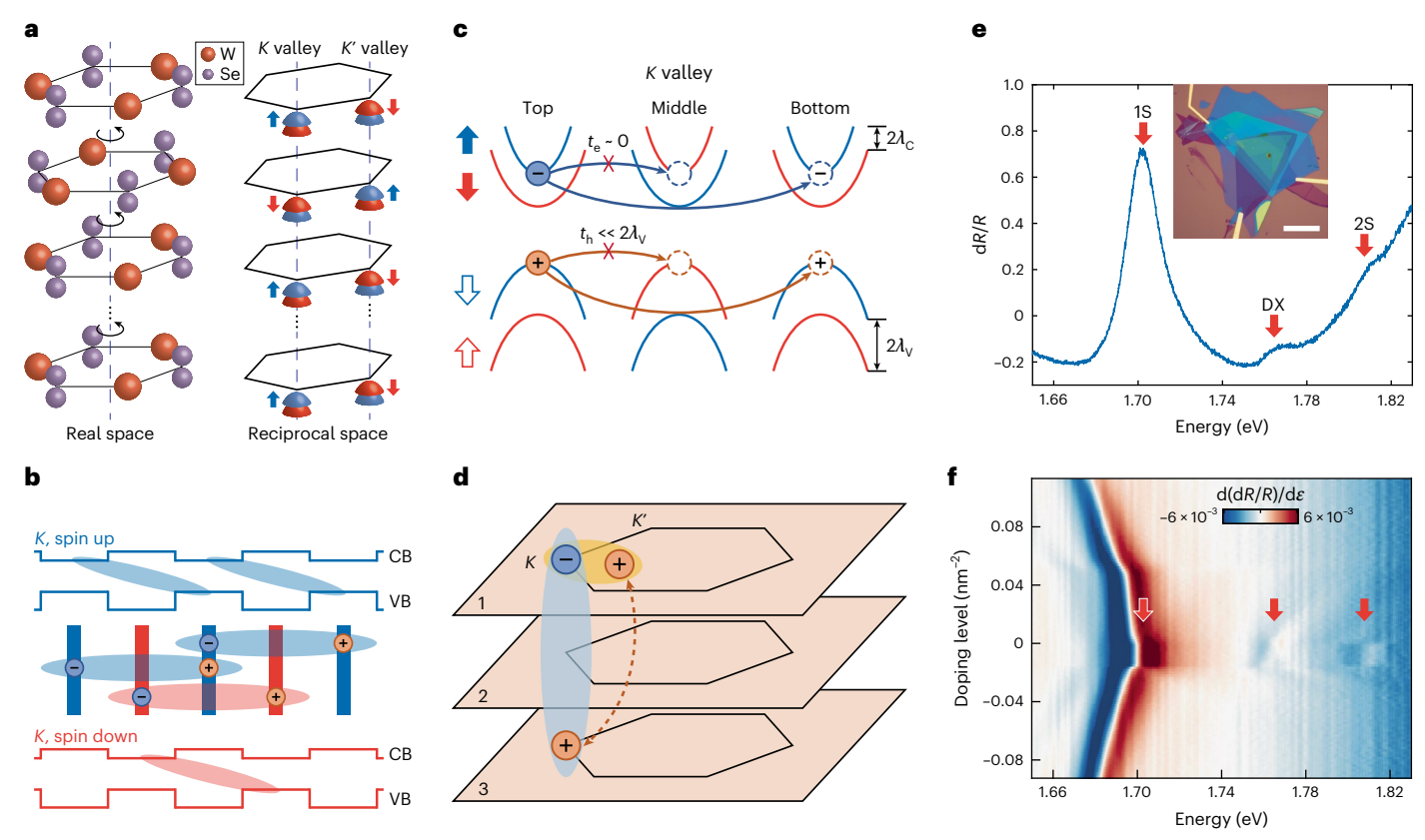


Fig. 1|**Spin-valley locked superlattice and every-other-layer exciton. a**, Crystal structure of multilayer 2H-WSe₂ in real space (left) and spin valley-coupled band edges in reciprocal space (right). Blue and red arrows stand for spin up and down, respectively. **b**, Schematic of the spin valley-dependent superlattice confinement of band edge carriers in 2H-WSe₂ multilayer and every-other-layer DXs. CB and VB denote the conduction band and valence band, respectively. Light blue and red ellipses represent DXs formed in odd and even layers, respectively. **c**, Interlayer hopping between adjacent layers is forbidden

due to spin-valley locking, while every-other-layer hopping is allowed. $t_{\rm e/h}$ denotes the hopping amplitude of electrons/holes. $\lambda_{\rm C/V}$ denotes the spin-orbit coupling strength of conduction/valence band. ${\bf d}$, Coupling between DX (light blue) and intralayer (orange) excitons in trilayer geometry. ${\bf e}$, Differential optical reflection spectrum (${\bf d}R/R$) from trilayer WSe $_2$ at charge neutrality and zero field. DX and intralayer 1S and 2S excitons are indicated by red arrows. The inset shows an optical microscope image of the dual-gated device. Scale bar, 20 μ m. ${\bf f}$, Doping dependence of differentiated dR/R from trilayer WSe $_2$ at zero electric field.

in the QW regions (Fig. 1b). Electrons see a lower barrier (-30 meV), but their interlayer hopping is forbidden at the $\pm K$ points by the rotational symmetry (Fig. 1c). These are reminiscent of the semiconductor superlattices from the periodical growth of two alternating III–V compounds, which underlie a broad range of important optical phenomena and applications but are now realized in a homogeneous compound featuring spin valley-dependent confinement (Fig. 1b).

In this work, we report the observation of a type of dipolar excitons (DXs) in such spin-valley locked superlattices in multilayer WSe $_2$. The DX, with electron and hole separated in an every-other-layer configuration, has a large electric dipole but vanishing optical dipole (Fig. 1d). However, it can become optically bright by hybridizing with the intralayer excitons via a weak next nearest neighbour interlayer hopping of carriers conserving spin and valley indices (Fig. 1c,d). We first present the results from a trilayer WSe $_2$ as the building block for such a superlattice: that is, a double QW.

Spectroscopic signature of every-other-layer DX

Figure 1e shows the differential reflectance spectrum normalized by the background reflectance (dR/R) in trilayer WSe_2 without applying gate voltage. The inset of Fig. 1e is the optical microscope image of the device, where the WSe_2 is sandwiched by hBN in a dual-gated geometry (Methods). The doping dependence of dR/R at zero electric field is shown in Fig. 1f. There are three resonances at charge neutrality, while the broad background at high energy is caused by optical interference.

The spectral features near 1.705 and 1.798 eV correspond to the 1S and 2S intralayer excitons, respectively $^{21-23}$. The 1S intralayer exciton state is schematically indicated in Fig. 1d by the electron–hole pair enclosed by the orange ellipses. Besides, there is a relatively weaker state at 1.767 eV, which is not seen from monolayer and bilayer WSe $_2$ spectra (Extended Data Fig. 1). The origin of this feature, corresponding to the every-other-layer DX with the electron–hole pair enclosed by the blue ellipses shaded in Fig. 1d, will become clear later in the electrical field-dependent measurements. The larger spatial separation of the electron and hole pair leads to a smaller binding energy of the DX compared with the intralayer 1S exciton and thus, higher energy in the optical spectrum.

We examine optical reflection versus the out-of-plane electric field $E_{\rm Z}$ at charge neutrality (Fig. 2a). The photoluminescence measurement is shown in Extended Data Fig. 2. As expected, the peak positions of both 1S and 2S intralayer excitons are independent of $E_{\rm Z}$. In contrast, the exciton feature at 1.767 eV evolves into two branches, whose energies shift linearly with $E_{\rm Z}$ and develop an X pattern centring at zero-field resonance. Since there are two energy-degenerate DXs but with opposite electric dipoles at $E_{\rm Z}$ = 0, the applied electric field breaks their degeneracy, linearly decreases (increases) the exciton energy and forms the observed X pattern. By fitting the stark effect, we can determine the electric dipole to be $d = \frac{\varepsilon_{\rm TMD}}{\varepsilon_{\rm BBN}} \frac{\Delta E_{\rm nergy}}{\Delta E_{\rm Z}} \approx 1.4 \, e\, {\rm nm} \; (e = 1.602 \times 10^{-19} {\rm C})$ using

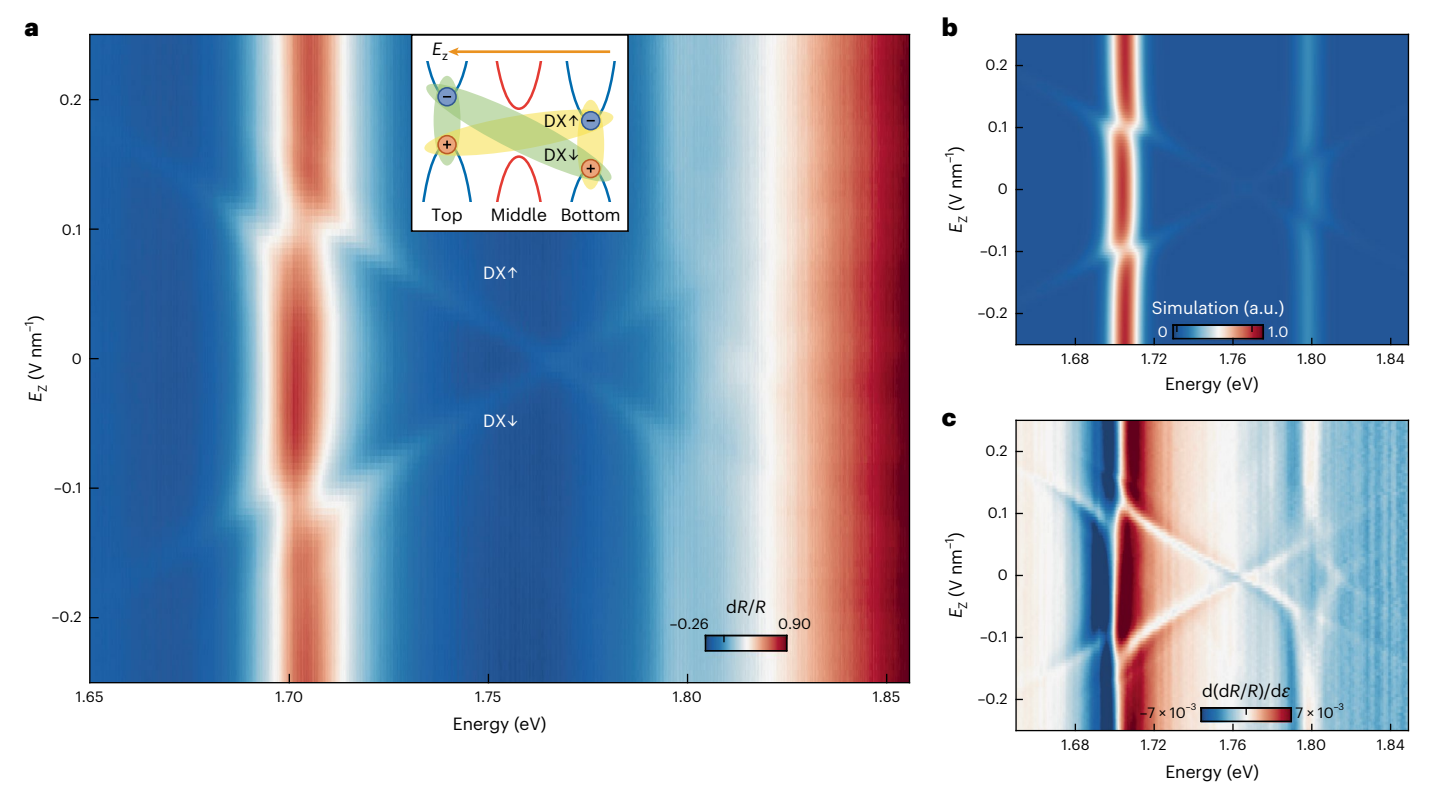


Fig. 2 | **Electric field tuning of exciton hybridization. a**, Electric field dependence of dR/R from trilayer WSe₂ at charge neutrality. The anti-crossing feature signifies the hybridization between DX and intralayer 1S and 2S excitons. DX, (DX_{\downarrow}) stands for DX with hole and electron in the top (bottom) and bottom (top) layers of the trilayer. The inset shows a schematic of energy bands and

exciton structures under positive electric field, where DX_+ can hybridize with the intralayer IS exciton close by in energy. **b**, Calculated electric field-dependent spectral density. **c**, Reflectance spectrum differentiated with respective to photon energy $(d(dR/R)/d\epsilon)$, where an excited state orbital of DX_{++} becomes visible as a higher-energy X pattern.

dielectric constants $\varepsilon_{TMD} \sim 7$ and $\varepsilon_{hBN} \sim 3$. This extracted dipole is exactly twice the usual interlayer exciton observed in heterobilayer TMDs, demonstrating that the electron and hole are now separated in every other layer.

Exciton hybridization

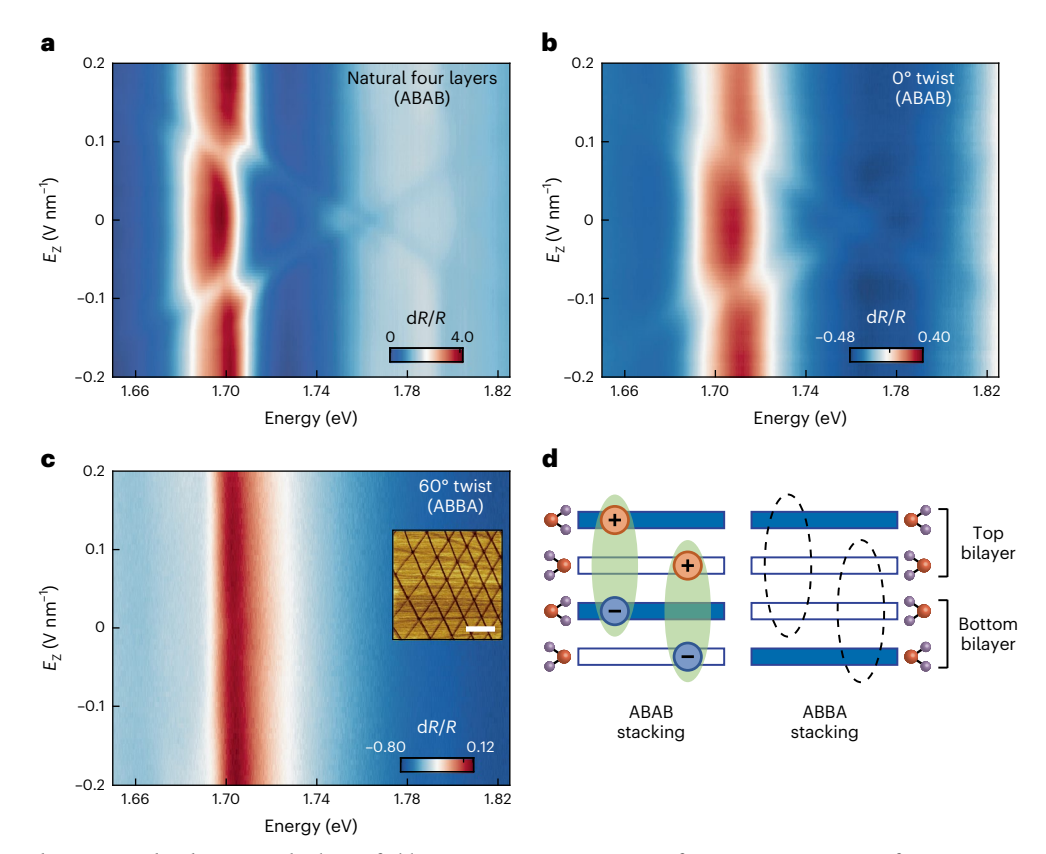
Figure 2a also shows several avoided-crossing features as the DX is tuned across the intralayer exciton resonances 24 . For instance, as E_Z is around $\pm 0.1 \, \text{V nm}^{-1} (\pm 0.06 \, \text{V nm}^{-1})$, the energy of the DX is nearly resonant with intralayer 1S (2S) excitons, where DXs hybridize with intralayer ones. This hybridization stems from the carrier hopping between layers 1 and 3 (Fig. 1c,d) and is crucial for the observation of the every-other-layer DX. We note that such DX has vanishing optical dipole by itself and becomes visible through hybridization with bright intralayer exciton states, even tens of millielectronvolts away from the 1S (2S) resonances.

To quantitatively understand the observation, we examine the coupling of the relevant exciton states: intralayer 1S and 2S excitons in layers 1 and 3 and the two DXs with opposite electric dipoles. The Hamiltonian is written as

$$H = \begin{pmatrix} \varepsilon_{1S} & 0 & t_1 & t_1 & 0 & 0 \\ 0 & \varepsilon_{1S} & t_1 & t_1 & 0 & 0 \\ t_1 & t_1 & \varepsilon_{DX} - E_Z \times d & 0 & t_2 & t_2 \\ t_1 & t_1 & 0 & \varepsilon_{DX} + E_Z \times d & t_2 & t_2 \\ 0 & 0 & t_2 & t_2 & \varepsilon_{2S} & 0 \\ 0 & 0 & t_2 & t_2 & 0 & \varepsilon_{2S} \end{pmatrix}. \tag{1}$$

Here, ε_{1S} , ε_{2S} and ε_{DX} denote the energies of intralayer and DXs at zero electrical field, extracted from Fig. 2a. The term $\pm E_Z \times d$ corresponds to the Stark shift of two DXs DX, ... The coupling between the DX and 1S (2S) intralayer exciton is through the carrier hopping with amplitude $t_1(t_2)$. $t_1(t_2)$ arises from the overlap in the envelope function of excitonic states and determines the anti-crossing gap near the 1S (2S) resonance. We found that $t_1 = t_2$ of about 5.5 meV best fits the eigenvalues versus E_Z to Fig. 2a. Given that every-other-layer DX has a rather different Bohr radius from that of the intralayer one, it is not that surprising that its envelope function can have comparable overlap with 1S and 2S envelope function of the intralayer exciton. After parametrizing the line width and emission intensity of the intralayer and DXs (Methods and Extended Data Fig. 3), the calculation well reproduces the differential reflectance spectra in Fig. 2b, which further supports our interpretation of the results.

We take the derivative of dR/R spectra in Fig. 2a versus the energy axis, $d\left(dR/R\right)/d\epsilon$. As shown in Fig. 2c, it reveals subtle spectral features. A second X pattern above the intralayer 2S state appears, centring at 1.813 eV. This X pattern exhibits the stark effect with the same slope corresponding to electric dipole $d\approx 1.4$ e nm. Therefore, we attribute this second anti-crossing to the higher orbital state of the every-other-layer exciton, which becomes visible through hybridizing with the intralayer 2S state. The energy separation between the ground and excited states of this every-other-layer DX is about 46 meV at $E_Z=0$, which sets the lower bound of the binding energy. In comparison with the intralayer 1S-2S exciton energy difference of about 93 meV, the binding energy of the DX is of the same order of magnitude. The observation of such a large energy scale for the every-other-layer binding is remarkable, which suggests that the screening effect in trilayer is still strongly suppressed.



 $\label{eq:Fig.3} \textbf{| Stacking-dependent every-other-layer DX. a, b,} \ Electric field dependence of dR/R from natural four-layer (a) and near-0° twisted double-bilayer WSe_2 (b). c, Electric field dependence of dR/R from near-60° twisted double-bilayer WSe_2. The inset shows that triangular domains appear in the$

piezo response force microscopy image of a near-60° twisted double-bilayer WSe $_2$ device. Scale bar, 200 nm. **d**, Cartoon of every-other-layer DX formation in double bilayers with ABAB stacking in comparison with the ABBA stacking.

Stacking dependence

Every-other-layer DX relies strongly on the spin-valley locked spin superlattice chain. If we break this periodicity in the stacking order, the DX can be switched off. For this purpose, we measured artificially twisted double-bilayer WSe₂ samples. Figure 3a,b shows the dR/R intensity plot of a naturally 2H-stacked four layer (Fig. 3a), near-0° twist (Fig. 3b) double bilayers and near-60° twisted double bilayers (Fig. 3c). In the natural four-layer sample, the X spectral pattern versus E_Z demonstrates the every-other-layer DX, which is formed between the layer number with the same parity: that is, either the first and third layers or second and fourth layers. A similar X pattern is observed in the 0° stacked double bilayers. In contrast, the 60° stacked double bilayers show drastically different spectra features compared with both naturally 2H and 0° twisted samples. As shown in Fig. 3c, only the 1S intralayer exciton is observed, which is insensitive to E_7 .

The 0° twisted sample resembles the natural four-layer WSe $_2$ in their ABAB stacking order, where each layer sits on top of another with 180° rotation (Fig. 3d). Due to the small twist angle between the double bilayers, moiré superlattices form at the interface between the two WSe $_2$ bilayers $^{25-27}$. In Fig. 3b, the intralayers 1S (1.706 eV) and 2S (1.803 eV) and DX (1.763 eV) states are all observed as well as the anti-crossing features near the intralayer 1S resonance. An electric dipole of 1.4 e nm is obtained, evidence for the every-other-layer configuration of the DX. Features from the 0° twist sample exhibit broader line width than the natural four-layer sample, possibly due to the inhomogeneity of 2H domain structures formed at the twisted interface. In comparison, the every-other-layer DX is absent from the 60° twisted double-bilayer WSe $_2$ (Fig. 3c). Different from 0° twisted

and natural four-layer samples, the 60° twisted sample is stacked in an ABBA order (Fig. 3d). The comparison of the two stacking further confirms our understanding of the spin-valley locked superlattices in the 2H structure, which is necessary for the formation of every-other-layer DX.

Layer number dependence

Finally, we examine DXs in samples with different thicknesses. We do not observe exciton feature with such a large electrical dipole in either monolayer or bilayer samples (Extended Data Fig. 1). This confirms that the basic unit for such an exciton is trilayer. In samples thicker than four layers, fine structures of multiple X patterns appear in the differential reflectance spectra. In a five-layer sample (Fig. 4a), there are two X patterns with a modest energy splitting of about 20 meV. Possible mechanisms to split the X pattern include a second-order carrier-hopping process, which couples two DXs through an intralayer exciton as the virtual intermediate state. We use DX_{ii} to denote the DX between the ith and ith layers. As schematically shown in Fig. 4c, through the hole-hopping process between the first and third layers, the DX D₁₃ is firstly coupled to the intralayer state at the third layer, which is then coupled to another dipole-up exciton DX₃₅ through an electron-hopping process between the third and fifth layers. However, given the carrier-hopping amplitude $t \sim 5.5$ meV we previously derived from fitting the trilayer WSe₂ spectra, the above second-order coupling process between two DXs is expected to give a smaller splitting than what we observed.

A more plausible explanation is the inhomogeneous dielectric environment along the vertical axis of the device stacking²⁸. The large layer separation of the every-other-layer DX leads to a larger Bohr

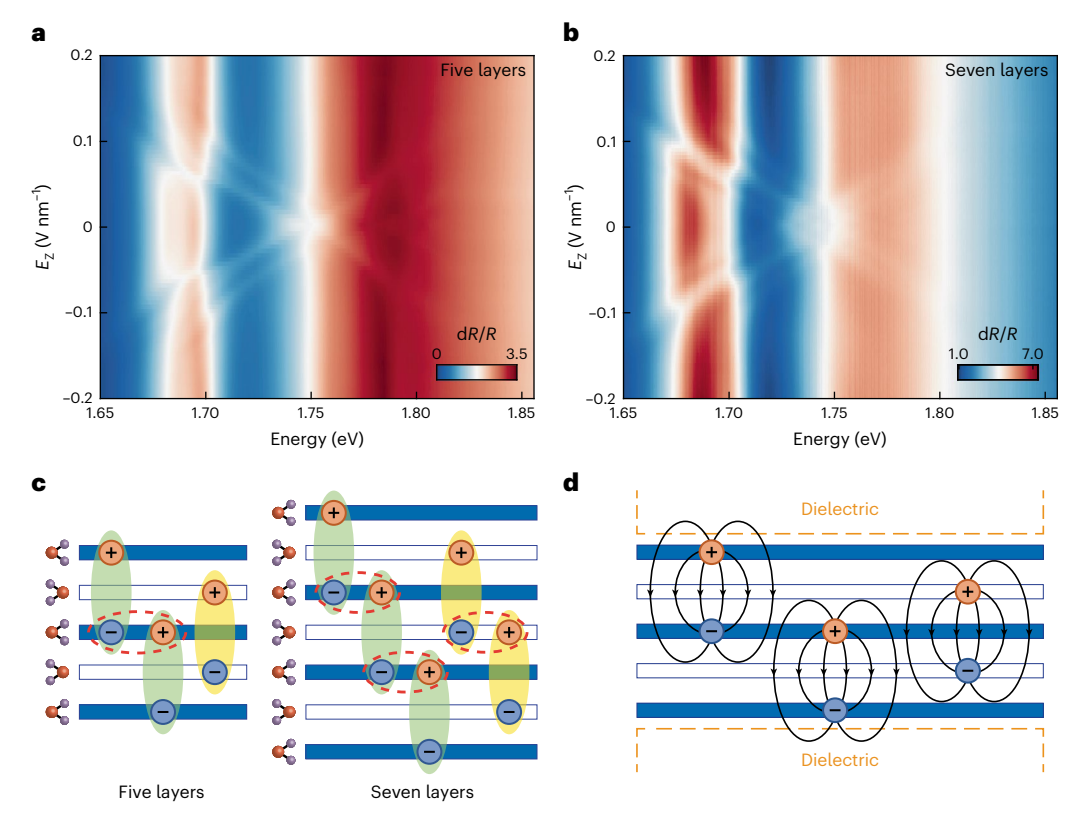


Fig. 4 | **Layer number dependence and multiple anti-crossings. a,b**, Multiple anti-crossings appear in the electric field dependence of d*R/R* from five-layer (**a**) and seven-layer (**b**) 2H-WSe₂. **c**, Hopping of DXs in the out-of-plane direction

through a virtual intralayer state in five and seven layers. Dashed red ellipses stand for the intralayer exciton states, which are coupled to two adjacent DXs. **d**, Illustration of different dielectric environment for DXs in a five-layer geometry.

radius, making it more sensitive to the surrounding dielectric environment. For example, comparing the DX_{13} and DX_{24} in a five-layer sample (Fig. 4d), the former is influenced more by the BN layers, which have different dielectric screening from the TMD layers. Such different dielectric environments for different DXs result in slight differences in their binding energies. Likewise, in a seven-layer sample, DX_{13} (DX_{57}), DX_{24} (DX_{46}) and DX_{35} will split into three different branches for the same reason, which agrees with what we observed in Fig. 4b. In comparison, in four-layer WSe $_2$, DX_{13} and DX_{24} do not couple to each other and have the same dielectric environment under the symmetric geometry with an hBN capping layer and substrate. The two thus have similar resonance energy (Fig. 3a).

Conclusions

Semiconductor superlattices underlie a broad range of fundamental science and technological applications; 2H-stacked TMD thin films host unique valleytronic superlattices, where even and odd layers form barriers and QWs depending on the spin-valley indices. In multilayer WSe₂, we found a DX with Coulomb-bound electron and hole in every-other-layer configuration, resulting in a large electrical dipole of 1.4 *e* nm, twice that of interlayer excitons in TMD heterobilayers. These DXs have tunable exciton hybridization, large binding energy and layer thickness-dependent spectroscopy features. Combined with the demonstrated layer stacking control, these findings may open avenues in engineering many-body effects of interacting bosons, as well as nanophotonics and quantum optoelectronics via valleytronic superlattice engineering.

Online content

Any methods, additional references, Nature Portfolio reporting summaries, source data, extended data, supplementary information,

acknowledgements, peer review information; details of author contributions and competing interests; and statements of data and code availability are available at https://doi.org/10.1038/s41565-023-01350-1.

References

- Bistritzer, R. & MacDonald, A. H. Moiré bands in twisted doublelayer graphene. Proc. Natl Acad. Sci. USA 108, 12233–12237 (2011).
- Cao, Y. et al. Unconventional superconductivity in magic-angle graphene superlattices. Nature 556, 43–50 (2018).
- Song, T. et al. Switching 2D magnetic states via pressure tuning of layer stacking. Nat. Mater. 18, 1298–1302 (2019).
- Li, T. et al. Pressure-controlled interlayer magnetism in atomically thin CrI₃. Nat. Mater. 18, 1303–1308 (2019).
- Yasuda, K., Wang, X., Watanabe, K., Taniguchi, T. & Jarillo-Herrero, P. Stacking-engineered ferroelectricity in bilayer boron nitride. Science 372, 1458–1462 (2021).
- Woods, C. et al. Charge-polarized interfacial superlattices in marginally twisted hexagonal boron nitride. *Nat. Commun.* 12, 347 (2021).
- Vizner Stern, M. et al. Interfacial ferroelectricity by van der Waals sliding. Science 372, 1462–1466 (2021).
- Xiao, D., Liu, G.-B., Feng, W., Xu, X. & Yao, W. Coupled spin and valley physics in monolayers of MoS₂ and other group-VI dichalcogenides. *Phys. Rev. Lett.* **108**, 196802 (2012).
- Jones, A. M. et al. Spin-layer locking effects in optical orientation of exciton spin in bilayer WSe₂. Nat. Phys. 10, 130–134 (2014).
- 10. Mak, K. F., He, K., Shan, J. & Heinz, T. F. Control of valley polarization in monolayer MoS_2 by optical helicity. *Nat. Nanotechnol.* **7**, 494–498 (2012).

- Wu, S. et al. Electrical tuning of valley magnetic moment through symmetry control in bilayer MoS₂. Nat. Phys. 9, 149–153 (2013).
- Zeng, H., Dai, J., Yao, W., Xiao, D. & Cui, X. Valley polarization in MoS₂ monolayers by optical pumping. Nat. Nanotechnol. 7, 490–493 (2012).
- Cao, T. et al. Valley-selective circular dichroism of monolayer molybdenum disulphide. Nat. Commun. 3, 887 (2012).
- Gong, Z. et al. Magnetoelectric effects and valley-controlled spin quantum gates in transition metal dichalcogenide bilayers. Nat. Commun. 4, 2053 (2013).
- Shi, Q. et al. Bilayer WSe₂ as a natural platform for interlayer exciton condensates in the strong coupling limit. Nat. Nanotechnol. 17, 577–582 (2022).
- Yankowitz, M., McKenzie, D. & LeRoy, B. J. Local spectroscopic characterization of spin and layer polarization in WSe₂. Phys. Rev. Lett. 115, 136803 (2015).
- Bawden, L. et al. Spin-valley locking in the normal state of a transition-metal dichalcogenide superconductor. *Nat. Commun.* 7, 11711 (2016).
- Slobodeniuk, A. O. et al. Fine structure of K-excitons in multilayers of transition metal dichalcogenides. 2D Mater. 6, 025026 (2019).
- Liu, G.-B., Shan, W.-Y., Yao, Y., Yao, W. & Xiao, D. Three-band tight-binding model for monolayers of group-VIB transition metal dichalcogenides. *Phys. Rev. B* 88, 085433 (2013).
- Wilson, N. R. et al. Determination of band offsets, hybridization, and exciton binding in 2D semiconductor heterostructures. Sci. Adv. 3, e1601832 (2017).
- Król, M. et al. Exciton-polaritons in multilayer WSe₂ in a planar microcavity. 2D Mater. 7, 015006 (2019).

- Arora, A. et al. Valley-contrasting optics of interlayer excitons in Mo- and W-based bulk transition metal dichalcogenides. Nanoscale 10. 15571–15577 (2018).
- Raiber, S. et al. Ultrafast pseudospin quantum beats in multilayer WSe₂ and MoSe₂. Nat. Commun. 13, 4997 (2022).
- Shimazaki, Y. et al. Strongly correlated electrons and hybrid excitons in a moiré heterostructure. Nature 580, 472–477 (2020).
- Yoo, H. et al. Atomic and electronic reconstruction at the van der Waals interface in twisted bilayer graphene. *Nat. Mater.* 18, 448–453 (2019).
- 26. Zhang, C. et al. Interlayer couplings, moiré patterns, and 2D electronic superlattices in MoS₂/WSe₂ hetero-bilayers. Sci. Adv. **3**, e1601459 (2017).
- McGilly, L. J. et al. Visualization of moiré superlattices. Nat. Nanotechnol. 15, 580–584 (2020).
- 28. Raja, A. et al. Coulomb engineering of the bandgap and excitons in two-dimensional materials. *Nat. Commun.* **8**, 15251 (2017).

Publisher's note Springer Nature remains neutral with regard to jurisdictional claims in published maps and institutional affiliations.

Springer Nature or its licensor (e.g. a society or other partner) holds exclusive rights to this article under a publishing agreement with the author(s) or other rightsholder(s); author self-archiving of the accepted manuscript version of this article is solely governed by the terms of such publishing agreement and applicable law.

© The Author(s), under exclusive licence to Springer Nature Limited 2023

Methods

Device fabrication

Flakes of hBN, graphite and WSe $_2$ are mechanically exfoliated from bulk crystals on Si/SiO $_2$ substrates. They are selected using an optical microscope and an atomic force microscope. The WSe $_2$ layer number is determined by an atomic force microscope and colour contrast, assisted by second-harmonic generation. The heterostructure is assembled layer by layer using a dry transfer technique. The twisted double-bilayer WSe $_2$ is fabricated using a 'tear-and-stack' technique, during which part of the bilayer WSe2 large flake is torn, picked up and stacked onto the remaining part with a twist angle that is precisely controlled by a rotary stage. Finally, the Cr/Au contacts are patterned with standard electron beam lithography and evaporation.

Optical measurements

The differential reflectance measurement is performed using a home-built confocal microscope in reflection geometry. The sample is mounted in an exchange-gas cooled cryostat with temperatures down to 5 K unless otherwise specified. A tungsten halogen white light source is used to excite the sample through a single-mode optical fibre. The beam diameter on the sample is about 1 μ m. The reflected light passes through a 50- μ m pin hole and is collected by a spectrometer with a silicon charge-coupled device. Polarization-resolved measurements are performed with a set of broadband half wave plates, quarter wave plates and linear polarizers. The differential reflection (d*R/R*) spectrum is obtained as d*R/R* \equiv (R' - R)/R by comparing the reflected light intensity from the sample (R') with that of a featureless spectrum (R) from the graphite–hBN–graphite area in the same sample.

Calibration of doping density and electric field

The doping densities in the heterobilayer are determined from the applied gate voltages based on a parallel-plate capacitor model²⁹. The thickness of hBN is determined by atomic force microscopy, typically around 10 to 20 nm thick. The doping density is calculated as $C_{\rm b}\Delta V_{\rm b} + C_{\rm t}\Delta V_{\rm t}$, where $C_{\rm t}$ and $C_{\rm b}$ are the capacitances of the top and bottom gates and $\Delta V_{\rm t}$ and $\Delta V_{\rm b}$ are the applied gate voltages relative to the level of the valence–conduction band edge. The geometric capacitance is calculated using $C_{\rm t,b} = \varepsilon_0 \varepsilon_{\rm BN}/d_{\rm hBN}$ with the dielectric constant of hBN $\varepsilon_{\rm hBN} \approx 3$ (ref. ³⁰). The out-of-plane electric displacement field is calculated using $D = (C_{\rm b}\Delta V_{\rm b} - C_{\rm t}\Delta V_{\rm t})/2\varepsilon_0$, and the electric field is calculated using $E_{\rm T} = D/\varepsilon_{\rm hBN}$.

Modelling and simulation

In trilayer, the relevant excitonic basis states for the observed hybridization are $|\mathrm{IS}^{top}\rangle,\,|\mathrm{IS}^{bottom}\rangle,\,|\mathrm{2S}^{top}\rangle,\,|\mathrm{2S}^{bottom}\rangle,\,|\mathrm{DX}_{\uparrow}\rangle$ and $|\mathrm{DX}_{\downarrow}\rangle$ denoting, respectively, the 1S and 2S orbital intralayer excitons in the top and bottom layers and every-other-layer DXs with electrical dipole pointing up and down. The diagonal part of the Hamiltonian can be written as

$$H_{0} = \begin{pmatrix} \varepsilon_{1S} & 0 & 0 & 0 & 0 & 0 \\ 0 & \varepsilon_{1S} & 0 & 0 & 0 & 0 \\ 0 & 0 & \varepsilon_{DX} - E_{Z} \times d & 0 & 0 & 0 \\ 0 & 0 & 0 & \varepsilon_{DX} + E_{Z} \times d & 0 & 0 \\ 0 & 0 & 0 & 0 & \varepsilon_{2S} & 0 \\ 0 & 0 & 0 & 0 & 0 & \varepsilon_{2S} \end{pmatrix}, \tag{2}$$

where $\pm E_Z \times d$ corresponds to the Stark shift of $|DX_{\downarrow\uparrow}\rangle$ away from their zero-field energy $\varepsilon_{\rm DX}$. Interlayer hopping of electron–hole leads to an off-diagonal coupling H_1 between $DX_{\downarrow\uparrow}$ and intralayer states (both 1S and 2S):

$$H_{1} = \begin{pmatrix} 0 & 0 & t_{1} & t_{1} & 0 & 0 \\ 0 & 0 & t_{1} & t_{1} & 0 & 0 \\ t_{1} & t_{1} & 0 & 0 & t_{2} & t_{2} \\ t_{1} & t_{1} & 0 & 0 & t_{2} & t_{2} \\ 0 & 0 & t_{2} & t_{2} & 0 & 0 \\ 0 & 0 & t_{3} & t_{3} & 0 & 0 \end{pmatrix}, \tag{3}$$

where t_1 (t_2) stands for the coupling strength between DX_{1↑} and the intralayer IS (2S) state.

After diagonalization of $H = H_0 + H_1$ by $H_D = U^{\dagger}HU$, we obtain six eigenstates $(|X_1\rangle, |X_2\rangle, |X_3\rangle, |X_4\rangle, |X_5\rangle, |X_6\rangle)$,

$$\begin{pmatrix}
|X_{1}\rangle \\
|X_{2}\rangle \\
|X_{3}\rangle \\
|X_{4}\rangle \\
|X_{5}\rangle \\
|X_{6}\rangle
\end{pmatrix} = U^{\dagger} \begin{pmatrix}
|1S^{top}\rangle \\
|1S^{bottom}\rangle \\
|DX_{\uparrow}\rangle \\
|DX_{\downarrow}\rangle \\
|2S^{top}\rangle \\
|2S^{bottom}\rangle
\end{pmatrix}, (4)$$

and eigenenergies $H_{\rm D}={\rm diag}\,(\varepsilon_1(E_{\rm Z}),\varepsilon_2(E_{\rm Z}),\varepsilon_3(E_{\rm Z}),\varepsilon_4(E_{\rm Z}),\varepsilon_5(E_{\rm Z}),\varepsilon_6(E_{\rm Z}))$ as a function of electric field. These to the base vectors, except around $\varepsilon_{\rm DX}\pm E_{\rm Z}\cdot d\approx \varepsilon_{\rm 1S/2S}$ regions, where DX_{1↑} hybridizes with intralayer 1S–2S and anti-crossing features appear. By fitting the resonance features in the measured dR/R data (red curves in Extended Data Fig. 3a), we obtain the coupling strength $t_1\approx t_2\approx 5.5\,{\rm meV}$.

We further model the spectral density of each excitonic state as a Gaussian distribution with a bandwidth w_i and intensity I_i ($i=1\text{S}^{\text{top/bottom}}$, $\text{DX}_{1/\uparrow}$, $2\text{S}^{\text{top/bottom}}$); the optical reflectance spectrum as a function of incidence energy ε and electric field E_z is given by

$$I(\varepsilon, E_z) = \sum_{j} \sum_{i} I_i |U_{ij}|^2 e^{-(\varepsilon - \varepsilon_j(E_z))^2/2\omega_i^2}.$$
 (5)

Extended Data Figure 3b is a plot using $f_{1S}^{\rm top} = f_{1S}^{\rm bottom} = 0.5$ $I_{\rm DX, L/\uparrow} = 0$, $I_{2S}^{\rm top} = I_{2S}^{\rm bottom} = 0.1$, $I_{2S}^{\rm top} = 0.5$ and $I_{2S}^{\rm top} = 0.5$ where we have assumed negligible optical oscillator strength of the every-other-layer DX. Nevertheless, DX_{1↑} states become visible through hybridization with intralayer 1S–2S states.

In five-layer WSe₂, the corresponding Hamiltonian becomes

$$H = H_0 + H_1 = \begin{pmatrix} H_{1S} & 0 & 0 \\ 0 & H_{DX} & 0 \\ 0 & 0 & H_{2S} \end{pmatrix} + \begin{pmatrix} 0 & H_{1S-DX} & 0 \\ H_{1S-DX}^{\dagger} & 0 & H_{2S-DX}^{\dagger} \\ 0 & H_{2S-DX} & 0 \end{pmatrix}, \tag{6}$$

where

$$H_{1S/2S} = \begin{pmatrix} \varepsilon_{1S/2S}^{(1)} & 0 & 0 & 0 & 0 \\ 0 & \varepsilon_{1S/2S}^{(2)} & 0 & 0 & 0 \\ 0 & 0 & \varepsilon_{1S/2S}^{(3)} & 0 & 0 \\ 0 & 0 & 0 & \varepsilon_{1S/2S}^{(4)} & 0 \\ 0 & 0 & 0 & 0 & \varepsilon_{1S/2S}^{(5)} \end{pmatrix}, \tag{7}$$

with $\varepsilon_{\rm 1S/2S}^{(l)}$ standing for the energy of intralayer 1S–2S exciton within the ith layer, and

$$H_{\rm DX} = \begin{pmatrix} \varepsilon_{\rm DX}^{(13)} & 0 & 0 & 0 & 0 & 0 \\ 0 & \varepsilon_{\rm DX}^{(31)} & 0 & 0 & 0 & 0 \\ 0 & 0 & \varepsilon_{\rm DX}^{(35)} & 0 & 0 & 0 \\ 0 & 0 & 0 & \varepsilon_{\rm DX}^{(53)} & 0 & 0 \\ 0 & 0 & 0 & 0 & \varepsilon_{\rm DX}^{(24)} & 0 \\ 0 & 0 & 0 & 0 & 0 & \varepsilon_{\rm DX}^{(42)} \end{pmatrix}, \tag{8}$$

with $\varepsilon_{\rm DX}^{(j)}$ standing for the energy of every-other-layer DX between the *i*th and *j*th layers.

 $H_{\rm IS-DX}$ ($H_{\rm 2S-DX}$) stands for the off-diagonal coupling between IS and DX (2S and DX) states through the electro or hole interlayer hopping:

$$H_{1S-DX/2S-DX} = \begin{pmatrix} t_{1/2} & t_{1/2} & 0 & 0 & 0 & 0 \\ 0 & 0 & 0 & 0 & t_{1/2} & t_{1/2} \\ t_{1/2} & t_{1/2} & t_{1/2} & t_{1/2} & 0 & 0 \\ 0 & 0 & 0 & 0 & t_{1/2} & t_{1/2} \\ 0 & 0 & t_{1/2} & t_{1/2} & 0 & 0 \end{pmatrix}. \tag{9}$$

Using the same fitting parameters $t_1 = t_2 = 5.5 \,\mathrm{meV}$ as in the trilayer case, the eigenenergies of the five-layer Hamiltonian are plotted as the red curves in Extended Data Fig. 3c. Note that considering the different dielectric environment of DX_{13/35} and DX₂₄, we have assigned different values to $\varepsilon_{\mathrm{DX}}^{(24/42)}$ and $\varepsilon_{\mathrm{DX}}^{(13/31/35/53)}$. Extended Data Figure 3d shows the optical spectrum, with the spectral intensity and width parameters $f_{\mathrm{IS}}^{(i)} = 0.2 f_{\mathrm{DX},1/1}^{(i)} = 0.f_{\mathrm{DS}}^{(i)} = 0.06$, $w_{\mathrm{IS}} = 5.5 \,\mathrm{meV}$ and $w_{\mathrm{2S}} = 4.5 \,\mathrm{meV}$.

Data availability

Source data are provided with this paper. All other data that support the plots within this paper and other findings of this study are available from the corresponding authors upon reasonable request.

References

- Wang, Z., Zhao, L., Mak, K. F. & Shan, J. Probing the spin-polarized electronic band structure in monolayer transition metal dichalcogenides by optical spectroscopy. *Nano Lett.* 17, 740–746 (2017).
- Movva, H. C. et al. Density-dependent quantum Hall states and Zeeman splitting in monolayer and bilayer WSe₂. Phys. Rev. Lett. 118, 247701 (2017).

Acknowledgements

This work was mainly supported by DoE BES (DE-SC0018171). Sample fabrication and PFM characterization were partially supported by the ARO MURI programme (W911NF-18-1-0431). The atomic force microscope-related measurements were performed using instrumentation supported by the US National Science Foundation through the UW Molecular Engineering Materials Center, a Materials Research Science and Engineering Center (DMR-1719797). W.Y. and C.X. acknowledge support from the University Grant Committee/ Research Grants Council of Hong Kong SAR (AoE/P-701/20 and HKU SRFS2122-7S05). W.Y. also acknowledges support from the Tencent Foundation. Bulk WSe₂ crystal growth and characterization by J.Y. were supported by the US Department of Energy, Office of Science, Basic Energy Sciences, Materials Sciences and Engineering Division. K.W. and T.T. acknowledge support from the JSPS KAKENHI (19H05790, 20H00354 and 21H05233). X.X. acknowledges support from the State of Washington-funded Clean Energy Institute and from the Boeing Distinguished Professorship in Physics.

Author contributions

X.X. and W.Y. conceived the project. Y.Z. fabricated samples and performed measurements assisted by D.O., J.Z. and X.W. Y.Z., X.X., C.X. and W.Y. analysed and interpreted the results. C.X. and W.Y. performed calculations. T.T. and K.W. synthesized the hBN crystals. J.Y. synthesized and characterized the bulk WSe $_2$ crystals. Y.Z., X.X., C.X. and W.Y. wrote the paper with input from all authors. All authors discussed the results.

Competing interests

The authors declare no competing interests.

Additional information

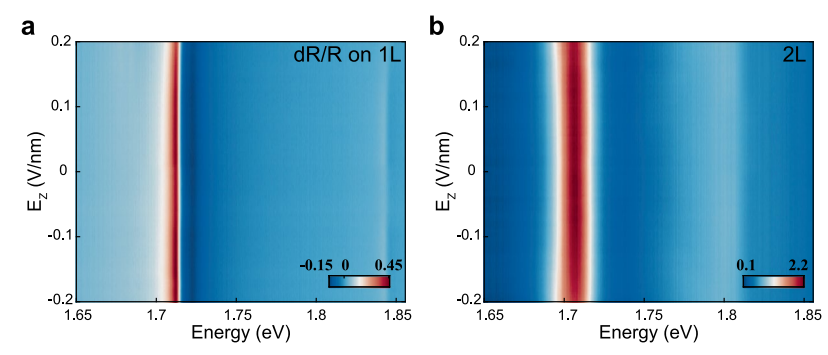
Extended data is available for this paper at https://doi.org/10.1038/s41565-023-01350-1.

Supplementary information The online version contains supplementary material available at https://doi.org/10.1038/s41565-023-01350-1.

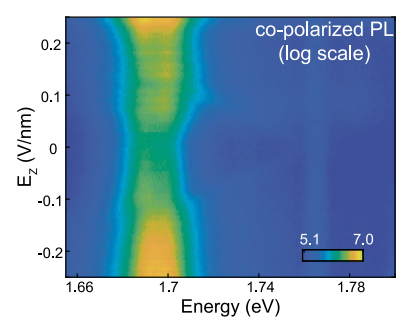
Correspondence and requests for materials should be addressed to Wang Yao or Xiaodong Xu.

Peer review information *Nature Nanotechnology* thanks the anonymous reviewers for their contribution to the peer review of this work.

Reprints and permissions information is available at www.nature.com/reprints.

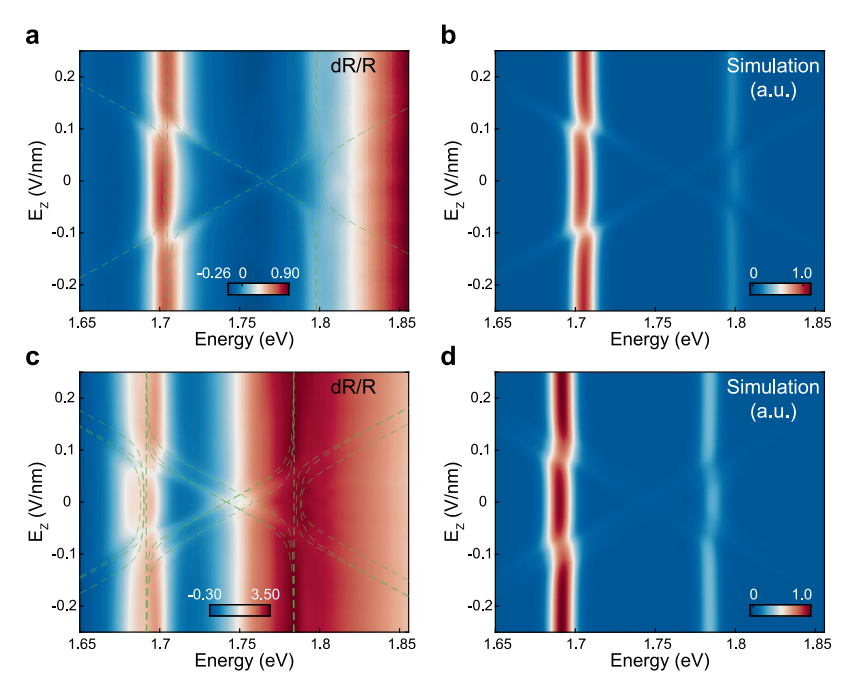


Extended Data Fig. 1 | Optical reflectance spectra in monolayer and bilayer WSe₂. a-b, Electric field (E₂) dependence of differential optical reflectance measurement in monolayer (a) and bilayer (b) WSe₂. Doping is fixed at zero. As expected, the every-other-layer dipolar exciton as well as the anti-crossing feature are not observed.



Extended Data Fig. 2 | Electric field E_z dependence of photoluminescence spectra in trilayer WSe₂. In addition to the dR/R data presented in the maintext, we examine photoluminescence (PL) spectra and its E_z field dependence on the same trilayer WSe₂. Near K-K direct transition region (around 1.7 eV), we

find similar anti-crossing feature as dR/R spectra, supporting the formation of every-other-layer dipolar excitons. The field-independent PL feature around 1.76 eV is instrument artefact.



Extended Data Fig. 3 | **Modeling and simulating the every-other-layer dipolar exciton. a, E_z** dependence of measured differential reflectance spectra in trilayer WSe₂. The green dashed lines show the curve fitting results based on the Hamiltonian Eq. (2) + (3). **b**, Simulation results after considering the spectral intensity and width. **c, d**, Same plots for 5-layer WSe₂.